Progress in PHOTOVOLTAICS

PROGRESS IN PHOTOVOLTAICS: RESEARCH AND APPLICATIONS
Prog. Photovolt: Res. Appl. 2014; **22**:452–461
Published online 1 October 2012 in Wiley Online Library (wileyonlinelibrary.com). DOI: 10.1002/pip.2291

RESEARCH ARTICLE

Characteristics of large-scale nanohole arrays for thin-silicon photovoltaics

Ting-Gang Chen[1], Peichen Yu[1]*, Shih-Wei Chen[2], Feng-Yu Chang[1], Bo-Yu Huang[1], Yu-Chih Cheng[1], Jui-Chung Hsiao[2], Chi-Kang Li[3] and Yuh-Renn Wu[3]

[1] Department of Photonics and Institute of Electro-Optical Engineering, National Chiao Tung University, Hsinchu 30010, Taiwan
[2] Green Energy and Environment Research Laboratories, Industrial Technology Research Institute, Hsinchu 31040, Taiwan
[3] Department of Electrical Engineering, National Taiwan University, Taipei 106, Taiwan

ABSTRACT

Nanostructured crystalline silicon is promising for thin-silicon photovoltaic devices because of reduced material usage and wafer quality constraint. This paper presents the optical and photovoltaic characteristics of silicon nanohole (SiNH) arrays fabricated using polystyrene nanosphere lithography and reactive-ion etching (RIE) techniques for large-area processes. A post-RIE damage removal etching is subsequently introduced to mitigate the surface recombination issues and also suppress the surface reflection due to modifications in the nanohole sidewall profile, resulting in a 19% increase in the power conversion efficiency. We show that the damage removal etching treatment can effectively recover the carrier lifetime and dark current–voltage characteristics of SiNH solar cells to resemble the planar counterpart without RIE damages. Furthermore, the reflectance spectra exhibit broadband and omnidirectional anti-reflective properties, where an AM1.5 G spectrum-weighted reflectance achieves 4.7% for SiNH arrays. Finally, a three-dimensional optical modeling has also been established to investigate the dimension and wafer thickness dependence of light absorption. We conclude that the SiNH arrays reveal great potential for efficient light harvesting in thin-silicon photovoltaics with a 95% material reduction compared to a typical cell thickness of 200 μm. Copyright © 2012 John Wiley & Sons, Ltd.

KEYWORDS
sub-wavelength structures; photovoltaic; solar cells; anti-reflection

***Correspondence**
Peichen Yu, Department of Photonics and Institute of Electro-Optical Engineering, National Chiao Tung University, Hsinchu 30010, Taiwan.
E-mail: yup@faculty.nctu.edu.tw

Received 2 January 2012; Revised 23 June 2012; Accepted 20 August 2012

1. INTRODUCTION

In recent years, solar energy plays an important role because of the rising cost of fossil fuels [1]. The majority of commercial solar cells are based on crystalline silicon for its non-toxic, abundant material resources, and long-term stability. Today's manufactured silicon solar cells have a typical thickness above 200 μm, which makes up to 40% of the total cost of the module [2]. As a result, the industry focuses on decreasing the wafer thickness and utilizing low-grade materials such as multi-crystalline silicon to bring down the cost. However, low-grade thin-silicon solar cells may suffer from several problems, including insufficient light absorption and poor carrier collection [3]. Therefore, new cell architectures need to be explored to address these issues. Over the past few years, nanostructured solar cells, in particular, silicon nanorods and nanoholes, have become a promising candidate for the evolution toward thin-substrate technologies [4–7]. The advantages of employing silicon nanostructures are multifold because of multiple efficiency enhancement mechanisms. The nanoscale textures buffer the abrupt refractive index difference between air and silicon via a tapered structural profile, offering broadband anti-reflection and light-trapping solutions to thin solar cells [8–11]. Moreover, the radial p–n junction configuration in nanostructures offers a perpendicular carrier collection path to the light absorption path, which allows the use of low-grade materials with a short diffusion length [12]. Among the proposed structures, the silicon nanohole arrays have theoretically shown better

 Copyright © 2012 John Wiley & Sons, Ltd.

light absorption than nanorods because of the strong optical diffraction and coupling [13,14]. However, the nanoscale texturing can only be beneficial when the enhanced light absorption surpasses the recombination via surface states due to increased surface area, which had rarely been investigated [15,16]. In this paper, we present the optical and photovoltaic characteristics of silicon nanohole solar cells. The fabrication of silicon nanohole arrays is demonstrated on a full 5-inch wafer using polystyrene nanosphere lithography and reactive-ion etching (RIE) techniques. A post-RIE wet etching is also introduced to remove the surface damages, which improves the surface reflection and internal quantum efficiency (IQE) considerably. Consequently, the short-circuit current density and power conversion efficiency are enhanced by 7.9% and 6.3%, respectively, compared with a NaOH-etched planar counterpart. Finally, a rigorous coupled-wave analysis (RCWA) method is also used to investigate the light absorption of SiNH arrays as a function of the periodicity, etch depth, and wafer thickness for thin-silicon photovoltaics.

2. METHODS

The fabrication of silicon nanohole arrays involved polystyrene nanosphere lithography followed by RIE. As illustrated in Figure 1, a 5-inch crystalline silicon wafer oriented along <100> with a thickness of 200 μm, and a resistivity of 0.6–10 Ω cm was first immersed in a 50% NaOH solution at 80 °C for 5 min for saw-damage removal and planarization. Next, polystyrene nanospheres were prepared at a purity of 10 wt% with an alcohol solvent and spun-cast on the silicon wafer with a spinning speed of ~3000 rpm to form a monolayer of nearly close-packed hexagonal arrays. The spheres were subsequently shrunken using RIE under a CHF_3/O_2 gas flow rate of 5/5 sccm to reduce the diameter, leading to hexagonal arrays that were no longer close-packed. The periodicity and diameter of nanohole arrays are determined by the original and reduced diameter of polystyrene spheres, which were 1 μm and 600 nm, respectively. Afterward, a 30-nm-thick nickel film was thermally evaporated as an etch mask, and the residual polystyrene spheres were removed with an ultrasonic alcohol bath. Here, an Anelva ILD-4100 helicon-wave etcher (Anelva. Corp., Tokyo, Japan) was used with a radio frequency and bias power of 1000 and 50 W, respectively, under a 5-mtorr pressure with 80-sccm CF_4. The etching rate was approximately 2 nm/s. During the etching process, the unprotected silicon was gradually etched away, and the remnant silicon formed nanohole arrays. The nickel film was then dissolved in a boiling nitric acid bath. Next, a damage removal etching (DRE) process was introduced to remove the ion-bombardment induced surface damages during plasma etching [17–19]. The etching of silicon was carried out from a two-step process: oxidation of silicon into SiO_2 by nitric acid and then dissolution of SiO_2 by HF. The DRE was performed in a solution mixture with a volume ratio of $HF:HNO_3:H_2O = 2:48:100$ for various etching times.

The fabricated SiNH and a planar reference substrates were then processed into cells via a conventional processing sequence. First, the p–n junction formation was performed in a quartz tube furnace with a liquid $POCl_3$ source at 900 °C, followed by dipping in dilute hydrofluoric acid to remove the phosphosilicate glass layer. After that, an 80-nm-thick silicon nitride (SiN_x) layer was deposited for surface passivation and also served as an anti-reflective coating using a plasma-enhanced chemical vapor deposition (PECVD) system. The PECVD system was operated

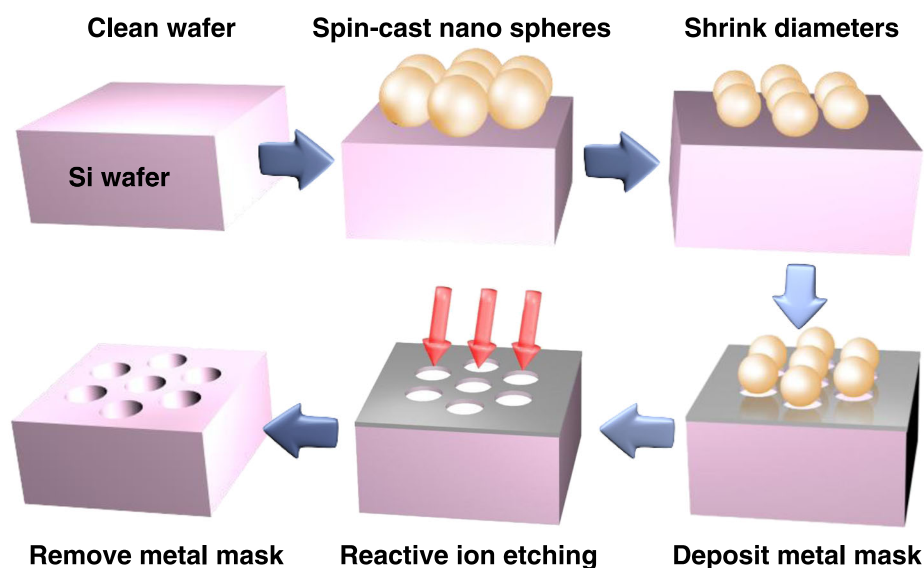

Figure 1. Schematic fabrication processes of silicon nanohole arrays.

with a radio frequency power of 35 W and a frequency of 13.56 MHz under a controlled pressure of 100 Pa at 300 °C. The gas flow rates for SiH_4, NH_3, and N_2 were 20, 10, and 490 sccm, respectively. The metallization was completed by screen printing with a silver grid and full-area aluminum for frontal and rear contacts, respectively. The cells were then sent to a fast-firing belt furnace with a peak temperature of 770 °C for electrode co-firing. Finally, the edge isolation was achieved with a 532-nm Nd:YAG laser scriber and the cell area was defined as 1.5 cm^2.

The junction profile was revealed by using a wet chemical technique based on the selective etching rate for layers with different doping concentrations, followed by a subsequent examination under a scanning electron microscope (SEM) [20]. The junction depth of the reference cell was first quantitatively characterized by using secondary ion mass spectroscopy (SIMS). Next, the planar reference and the nanohole solar cell with a 10-s DRE treatment are dipped in a mixture with a volume ratio of HF (49%) : HNO_3 (65%) : CH_3COOH (100%) = 3:6:16 for 2 s, respectively. In both samples, the SiN_x passivation layer serves as a protection layer to ensure that the etching takes place on the cross-section instead of the front surface.

The power conversion efficiency was carried out by using a class A solar simulator with an illumination condition of 1000 W/m^2 for the AM1.5 G solar spectrum. The temperature was maintained at 25 ± 1 °C by using a balanced cooling water and heat plate system. Before measurement, the intensity was calibrated with a reference cell from Fraunhofer Inc. (Plymouth, MI, USA) to ensure that the irradiance variation is within 3%. The external quantum efficiency (EQE) system used a 300 W Xenon light source (Newport Inc., Irvine, CA, USA) with a spot size of 1 mm × 3 mm and calibrated with a silicon photodetector from Newport (Irvine, CA, USA). The angle-resolved reflectance measurement was performed with a motor-controlled rotational stage and an integrating sphere to collect the specular and diffused reflected light at various angles of incidence (AOIs).

3. RESULTS AND DISCUSSION

We used nanospheres with a diameter of 1 μm to define the periodicity and subsequently reduced to 600 nm for the nanohole diameter. The depths were chosen to be 350, 600, and 1800 nm, controlled by adjusting the etching time for 180, 300, and 1000 s, respectively. The morphology of fabricated SiNH arrays was examined using a SEM and shown in Figure 2. First, Figure 2(a) shows the uniformly distributed shrunken polystyrene nanospheres in a hexagonal arrangement. Figure 2(b and c), respectively, shows SiNH arrays with both a diameter and depth of 600 nm from fabricated cells *before* and *after* the DRE treatment (10 s). The insets show the

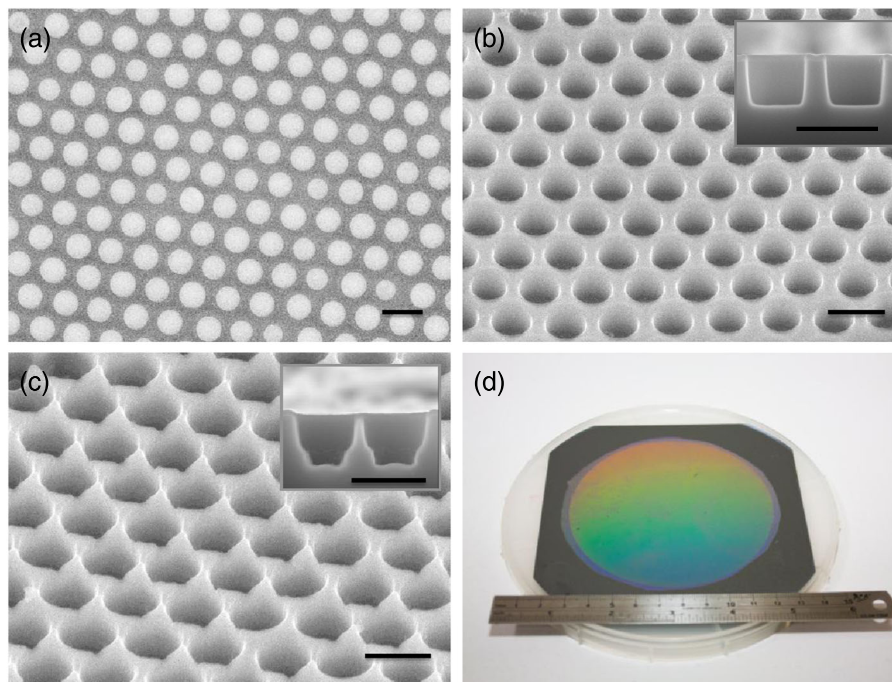

Figure 2. Scanning electron microscopic images of (a) polystyrene nanosphere arrays with a period of 1 μm and a diameter of 600 nm. (b) The fabricated SiNH arrays with a diameter and a depth of both 600 nm. The inset shows a cross-sectional view. (c) The condition of (b) with an additional 10-s damage removal etching (DRE). The inset shows the sidewall profile after DRE. (d) Photograph of fabricated SiNH arrays demonstrated on a 5-inch wafer, where the light dispersion indicates the uniformity across the full wafer. Scalar bars are in 1 μm.

DOI: 10.1002/pip

corresponding cross-sectional view of side walls. Because of an isotropic etching mechanism in the nitride acid and HF solution, the top edges of the nanohole have a relatively high etching rate, leading to a tapered sidewall profile. Figure 2(d) shows a photograph of the fabricated SiNH arrays with a 4-inch circular area on a 5-inch wafer. The grating-like light dispersion indicates the uniformity of the process, which is scalable for large-area solar cell manufacturing. The cross-sectional junction profile is demonstrated via a selective wet chemical etching technique, where the etched cross-sectional morphology of the planar reference cell is shown in Figure 3(a). We observe two iso-concentration lines (dotted lines) at depths of approximately 150 and 300 nm. Overlaying the SEM picture with a SIMS data of the same cell makes the two yellow dotted lines correspond to a doping concentration of ~1×10^{19} and ~6×10^{17} cm^{-3}. On the basis of the SIMS data, as the gradient of the doping concentration within the first 100 nm is very sharp and the pre-deposition of the P_2O_5 dopant layer on the nanostructured surface may not be uniform, the doping profile of nanoholes after the drive-in process is difficult to predict. Nevertheless, the selective etching technique can still reveal two iso-concentration contours (dotted lines) on the cross-section of the fabricated silicon nanohole sample with a 10-s DRE treatment, as shown in Figure 3(b), after quickly etching for 2 s. The selectively etched arc profiles confirm that a graded doping concentration indeed occurs around the sidewalls of nanoholes, indicating a partial radial field distribution for carrier separation and collection. Further characterizations are still required to determine the junction depth.

We first show the current–density voltage, reflectance, and EQE characteristics of SiNH cells with different aspect ratios before the DRE treatment in Figure 4(a and b). The measured SiNH cells have a periodicity and a diameter of 1 µm and 600 nm, respectively, and various etch depths of 350, 600, and 1800 nm. As seen in Figure 4(a), all the samples perform worse than the reference cell with a NaOH-etched planar surface. Both the open-circuit voltage and the short-circuit current density are decreased with the increased nanohole depth because of increased surface defects. Nevertheless, as seen in Figure 4(b), the deeper nanoholes exhibit lower surface reflection than the

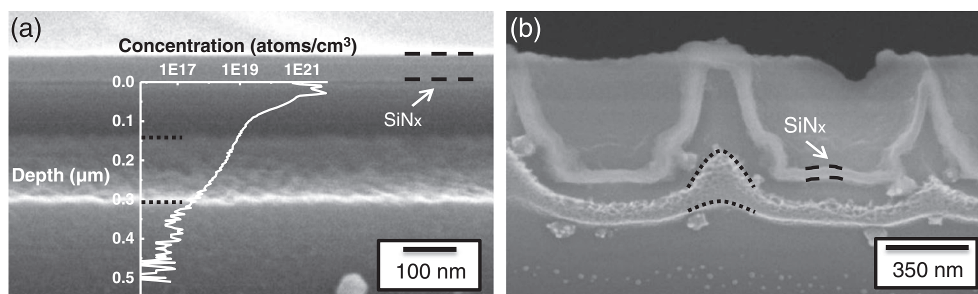

Figure 3. Delineation of the junction profile by using a wet chemical-selective etching technique: (a) the planar reference cell overlaying the dopant profile obtained by a secondary ion mass spectroscopy, and (b) the SiNH solar cell with a 10-s damage removal etching treatment. The dotted lines denote the two iso-concentration contours.

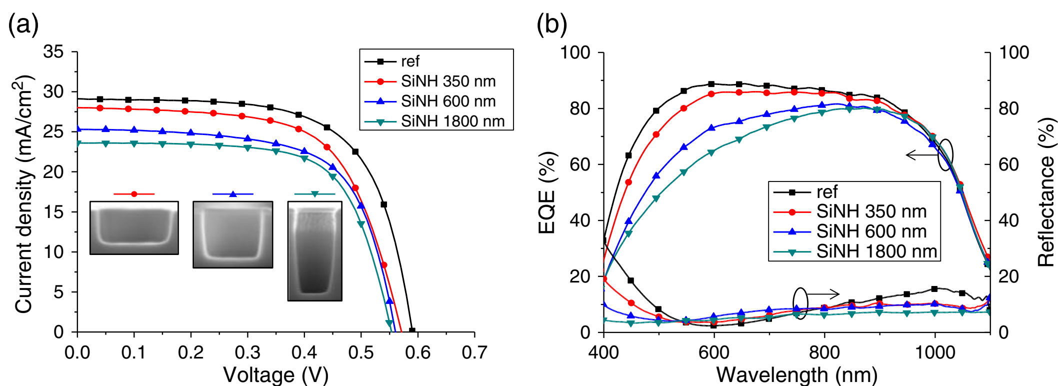

Figure 4. (a) The current–density voltage characteristics, (b) the external quantum efficiency (EQE), and reflectance spectra of SiNH solar cells with a diameter of 600 nm and various etch depths of 350, 600, and 1800 nm. A NaOH-etched planar counterpart is used as the reference. The insets show the cross-sectional images corresponding to the data lines.

reference, particularly for wavelength below 500 nm and above 800 nm. The lowered reflectance for SiNH samples is not reflected in the photocurrent output. The EQE analysis (Figure 4(b)) further shows the deterioration of short-circuit current density occurred in the short-wavelength range, indicating that the photogenerated carriers are recombined at nanohole surfaces and reduced the IQEs of the cells. Moreover, as the nanohole surface is also a heavily doped n-type layer, the Auger recombination may also take place, leading to a decreased photocurrent. Similar characteristics have been observed for crystalline silicon solar cells with nanowire surface textures using a silver-induced etching technique [21,22]. However, we believe that the surface recombination in our device is dominant, as the IQE characteristics are almost recovered after the DRE.

In general, the silicon surface exposed to RIE suffers from physical and chemical damages. These damages include ion bombardment, radiation damages by UV photons and high energy electrons as well as chemical residues contamination, and polymer formation by chemical species. The damaged silicon surface consists of a thin plasma residual layer followed by a lattice-damaged Si layer and a plasma impurity-diffused layer [23]. Therefore, proper surface treatments and passivation methods are necessary to overcome the surface damage-induced performance degradation. However, conventional methods such as annealing and thermal oxide involving a high temperature process tend to degrade the wafer quality [24]. Directly stripping the damaged Si surface by wet chemical etching is the most effective way to improve the surface quality [25]. Among various options, anisotropic alkaline etching such as KOH and NaOH were avoided because of texturing the planar surface and attacking nanostructures. Isotropic etching involving an oxidation and dissolution process in HF/ HNO_3/H_2O solutions was therefore preferred for the DRE. Figure 5 shows the solar cell performance of SiNH arrays *with* and *without* the DRE treatment for 5 and 10 s. The SiNH dimensions are referred to Figure 2(b) with an etch depth of 600 nm. Figure 5(a) shows the measured current–voltage characteristics of the best performing cells. The averaged characterizations of three devices and the error ranges are presented with a calculated 95% confidence interval in Table I. We observe a clear

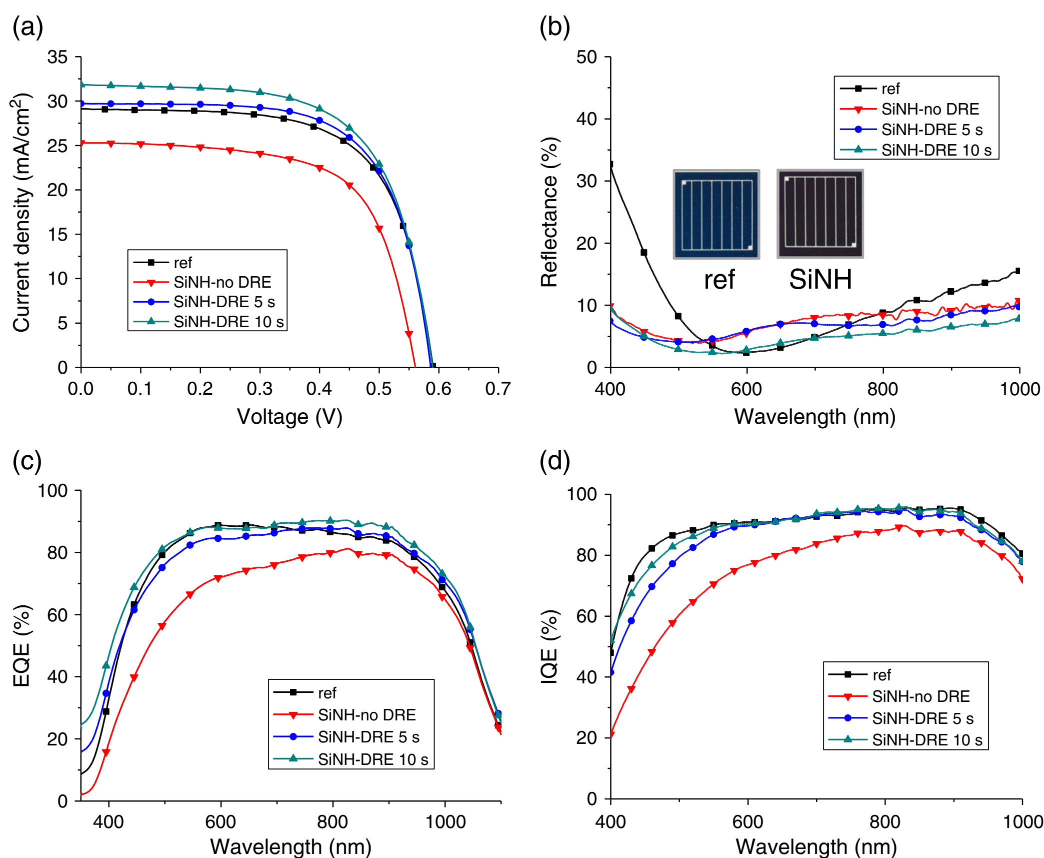

Figure 5. Characteristics of the reference and SiNH cells *with* and *without* the damage removal etching (DRE). (a) The current–density voltage under a simulated 1-sun AM1.5 G illumination. (b) The reflectance spectra at normal irradiance measured with an integrating sphere. The insets show the photographic images of fabricated cells. (c) The measured external quantum efficiency (EQE) and (d) extracted internal quantum efficiency (IQE) spectra using the expression, IQE = EQE/(1 − R).

Table I. The current–voltage characteristics of the reference and SiNH solar cells *with* and *without* the DRE treatment.

Structure	V_{oc}* (V)	J_{sc}* (mA/cm^2)	Fill factor* (%)	Efficiency* (%)
Reference	0.590 ± 0.003	29.2 ± 0.1	64.8 ± 0.8	11.2 ± 0.2
SiNH (no DRE)	0.561 ± 0.002	25.2 ± 0.2	66.1 ± 2.0	9.34 ± 0.4
SiNH (DRE 5 s)	0.587 ± 0.004	29.1 ± 0.7	64.9 ± 1.4	11.1 ± 0.5
SiNH (DRE 10 s)	0.590 ± 0.003	31.5 ± 0.3	64.1 ± 0.8	11.9 ± 0.2

*The statistics present the error range of three measured samples with a 95% confident interval.

improvement in the open-circuit voltage (V_{oc}) and short-circuit current density (J_{sc}) with the DRE treatment. The measured reflectance spectra at normal illumination incidence are shown in Figure 5(b), where the reflectance of SiNH reveals a broadband anti-reflective property. The insets show the photographs of the reference cell and the SiNH cell with a depth of 600 nm with a DRE time of 10 s. The reference cell exhibits a blue surface because of high reflectance at 400~500 nm wavelengths, which is typical with a standard single-layer anti-reflective coating designed for destructive interference at 600 nm. In contrast, the SiNH cell appears deep black to human eyes. As shown in Figure 2(c), the reduced reflectance results from a change of morphologies, which better fit to a graded refractive index profile [26]. The EQE spectra shown in Figure 5(c) demonstrate that the DRE treatment can effectively recover the short-wavelength response. As a result, the photogenerated current and power conversion efficiency are much enhanced, compared with those without the DRE treatment, and also superior to the planar reference counterpart. To decouple the influence of optical absorption and carrier collection properties *with* and *without* the DRE treatment, IQE spectra are also calculated using the expression: IQE = EQE/(1 − R). The IQE is defined as the number of carriers collected to that of photons absorbed in the active layer. The surface and bulk recombination loss can therefore be analyzed in the IQE spectra. As shown in Figure 5(d), the reduced IQE due to dry etch is recovered with the DRE treatment, where the improvement is positively correlated with the treatment time. Moreover, it can be seen that the IQE improvement mainly lies on the blue side of the spectra. As the short-wavelength photons are mostly absorbed on the surface because of high absorption coefficient, the amount of surface defects plays an important role in the collection of short-wavelength photogenerated carriers. By directly stripping the damaged Si surface and sub-surface layer using wet chemical etching, we can recover the IQE characteristics closer to those of the planar reference, which did not involve dry etching.

The recovery of surface conditions with the DRE treatment is further supported by an effective carrier lifetime measurement via microwave reflection photoconductance decay (μ-PCD) for SiNH arrays covered with a SiN_x layer. The measurement uses a laser with a wavelength of 904 nm at an injection level of $10^{15}\,cm^{-3}$, and the average lifetimes of the planar reference, SiNH without DRE, and with DRE for 5 and 10 s are summarized in Table II. The planar reference shows an effective lifetime of 25.5 μs, in contrast to 17.5 μs for SiNH arrays without DRE. As shown in Table II, the carrier lifetime is gradually improved and reaches 23.0 μs after a 10-s DRE treatment, which is closer to that of the planar reference when taking into account the increased surface area of nanoholes. Similarly, the surface conditions of SiNH solar cells can also be reflected in the dark current–density voltage characteristics, as shown in Figure 6(a). We extract the ideality factor as a function of the bias voltage using Equation (1) for various SiNH samples and plotted in Figure 6(b):

$$\frac{1}{n} = \left(\frac{kT}{q}\right)\left(\frac{\mathrm{d}\ln J_{dark}}{\mathrm{d}V}\right) \tag{1}$$

where n is the ideality factor, k is the Boltzmann constant, T is the temperature, q is the charge of an electron, J_{dark} is the measured current density in dark, and V is the bias voltage. As shown in Figure 6(a), the linear current characteristics at the reverse bias and the large ideality factor ($n > 2$) at forward bias in Figure 6(b) indicate the occurrence of multiple recombination mechanisms besides the Shockley–Read–Hall recombination. Several studies have identified that the origins of current with $n > 2$ are edges and local non-linear shunts on the surface [27,28]. Because of the small cell area, the fabricated cells including the planar reference have a large perimeter-to-area ratio, where the edge recombination current induced by laser cut damages is considerable, leading to non-ideal diode behaviors. Moreover, we can also see that the peaks of ideality factors for SiNHs without the DRE treatment are shifted towards high bias, compared with the planar counterpart. As surface damages result in mid-gap defect levels, this phenomenon can be well explained

Table II. Effective carrier lifetime of the planar reference and SiNH arrays with different DRE times.

Structure	Effective lifetime (μs)
Reference	25.5
SiNH (no DRE)	17.5
SiNH (DRE 5 s)	21.6
SiNH (DRE 10 s)	23.0

DOI: 10.1002/pip

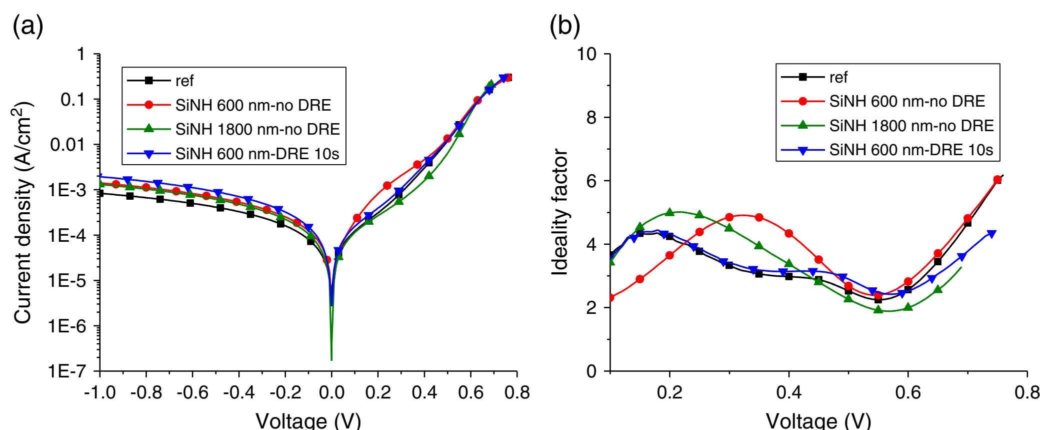

Figure 6. (a) Dark current–density voltage characteristics of the planar reference, SiNH cells with different etch depths, and the SiNH cell involving a 10-s damage removal etching (DRE) treatment. (b) Bias-dependent ideality factors extracted from the dark diode characteristics.

by recombination via deep donor–acceptor pairs occurring in heavily defected regions induced by the mechanical damages of RIE [29]. Therefore, by stripping away the damaged surfaces, the ideality factors of the SiNH cell involving the DRE treatment become similar to those of the planar reference again, and the diode properties in dark are recovered compared with the sample without RIE damages.

To summarize the photovoltaic characteristics of SiNH solar cells, it is worth noting that the suppressed surface reflection and recombination via the DRE treatment play a more important role than the formation of a radial junction profile in the present SiNH solar cells. Although Figure 3(b) reveals an arc junction profile around the sidewalls of the nanohole array, it is challenging to precisely control the doping depth in forming a nanoscale core–shell junction via $POCl_3$ diffusion. Because the fabricated SiNH solar cells use a monocrystalline silicon wafer with a doping concentration of ~5×10^{15} cm^{-3} and a diffusion length above 100 µm, the measured photocurrent mostly comes from bulk absorption, and the demand for a radial field is relieved. However, the proposed DRE method is essential and fully compatible to the fabrication of silicon nanostructures involving core–shell junctions and low-grade materials.

Another unique optical property for SiNH arrays is their omnidirectional anti-reflection. Sunlight impacts to the solar panel with a gradually rotational incident angle, about 15°/h and reaches normal incidence with respect to solar panel at noon. Therefore, in a non-tracking system, the reflectance needs to maintain low at various incident angles for sustained electricity production for the entire day. To analyze the reflectance characteristics at different angles of incidence, the angle-resolved reflectance spectra were measured for the reference and the SiNH cell with a 10-s DRE treatment as shown in Figure 7(a and b), respectively. The color bars represent the reflectance from low (blue) to high (red). The SiNH cell exhibits broadband low reflectance not only at normal incidence but also at large AOIs, represented by the enlarged blue area. To obtain an overall figure of merit, we calculated the AM1.5 G solar spectrum-weighted reflectance for various SiNH samples as a function of the AOI up to ±60°, which corresponds to the sun position from 8 A.

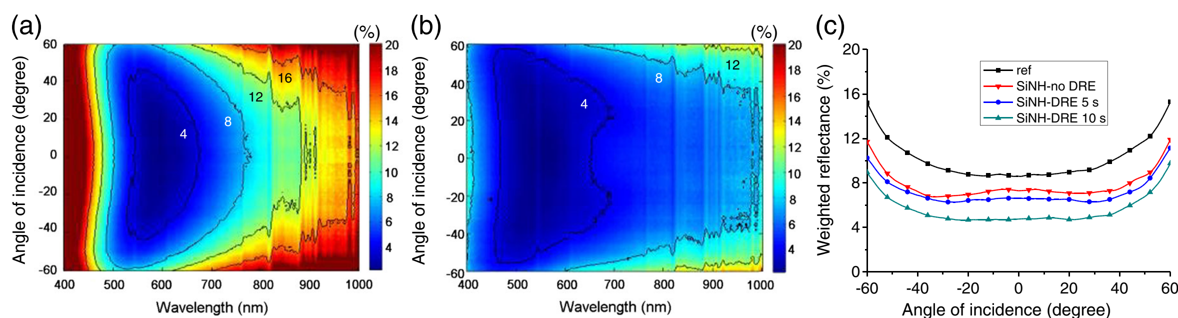

Figure 7. The measured angle-resolved reflectance spectra of (a) the flat reference and (b) the SiNH arrays with a damage removal etching (DRE) treatment for 10 s. (c) The AM1.5 G spectrum-weighted reflectance as a function of irradiance incident angles for the flat reference and SiNH arrays with and without the DRE treatment.

 Prog. Photovolt: Res. Appl. 2014; **22**:452–461 © 2012 John Wiley & Sons, Ltd.
DOI: 10.1002/pip

M. to 4 P.M. The AM1.5 G solar spectrum-weighted reflectance is calculated using Equation (2):

$$< R(\theta) >= \frac{\int_{400\mathrm{nm}}^{1000\mathrm{nm}} R(\lambda,\theta) I_{\mathrm{AM1.5G}}(\lambda)\mathrm{d}\lambda}{\int_{400\mathrm{nm}}^{1000\mathrm{nm}} I_{\mathrm{AM1.5G}}(\lambda)\mathrm{d}\lambda} \qquad (2)$$

where $R(\lambda, \theta)$ is the measured reflectance at an incident angle of θ and wavelength λ; $I_{AM1.5G}$ is the photon flux density of the AM1.5 G spectrum [30]. $<R(\theta)>$ denotes the weighted angular reflectance over the wavelength range of $\lambda = 400$ to 1000 nm, as shown in Figure 7(c). At the normal illumination incidence, the reference and the SiNH samples with various DRE times: 0, 5, and 10 s exhibit $< R > = 8.6\%$, 7.3%, 6.6%, and 4.7%, respectively. It is clear that the SiNH array with a 10-s DRE treatment shows the best broadband and omnidirectional anti-reflective properties, which are very suitable for the daily operation of solar panels.

Optical management for single or multi-crystalline silicon solar cells today may soon face two challenges when wafer thickness is reduced below 100 µm. First, the microscale-texturizing technique commonly used for the commercial products may restrain its applicability to thin silicon with a thickness of only tens of micrometers. Second, the anisotropic etching mechanism is also not preferred for multi-crystalline silicon because of randomly distributed crystal orientations. The SiNH arrays hold great potential as a substitute surface texture for low-grade thin-silicon solar cells. To further estimate the potential value for light harvesting of the SiNH arrays in thin-silicon film, an RCWA method was developed to calculate the wafer thickness dependence of photocurrent output. The RCWA technique is widely used to analyze the forward and backward diffraction of electromagnetic waves propagating through periodic sub-wavelength structures, such as gratings and photonic crystals [31,32]. In the simulation, we choose an equal amount of transverse-electric and transverse-magnetic polarizations to represent the randomly polarized sunlight in order to model nanostructures with polarization-dependent optical properties. As schematically shown in Figure 8

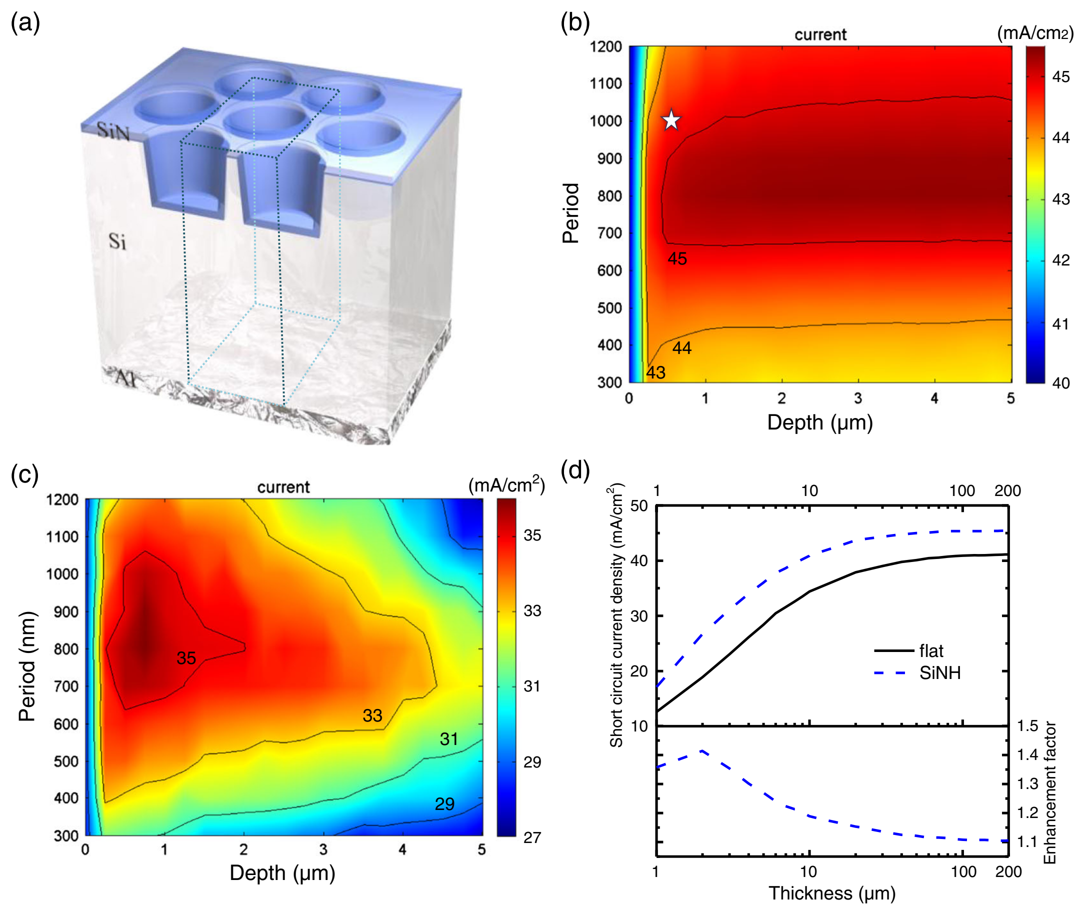

Figure 8. (a) Schematic illustration of the three-dimensional optical model. The dotted box represents the simulated unit cell to comply with the periodic boundary condition. (b) The calculated photocurrent density J_{sc} of SiNH cells as a function of the periodicity and the etch depth for a 200-µm-thick and (c) for a 5-µm-thick wafer. The white star denotes the dimensions of fabricated SiNH cells. (d) The wafer thickness dependence of J_{sc} and the corresponding enhancement factor defined as $J_{sc,SiNH}/J_{sc,\ flat}$.

(a), a three-dimensional optical model was constructed with close-packed hexagonal nanohole arrays, where the simulated unit cell is indicated in a dotted box to comply with the periodic boundary conditions on the horizontal plane. The model includes a SiN_x anti-reflective layer with the measured material refractive index obtained from an n&k analyzer (n&k Technology, Inc., San Jose, CA, USA) and an aluminum rear contact for back reflection with parasitic absorption taken into account. The calculated absorption of the silicon active layer was then expressed as the short-circuit current density by integrating over the AM1.5 G spectrum using the following Equation (3):

$$J_{sc} = \frac{e}{hc}\int_{300}^{1200} \lambda \times IQE(\lambda) \times [Abs_{sim}(\lambda)] \times I_{AM1.5G}\, d\lambda \quad (3)$$

where e is the charge of an electron, h is Plank's constant, c is the speed of light, $I_{AM1.5G}$ is the intensity of AM1.5 G spectrum, and Abs_{sim} represents the calculated absorption of silicon nanoholes. Here, the IQE(λ) was assumed to be unity as an ideal situation that all absorbed photons are contributed to current output without losses. Hence, the absorption ability can be directly evaluated by the calculated J_{sc} values. We first investigate the dimension dependence of the output photocurrents from SiNH arrays with two different wafer thicknesses of 200 and 5 μm. As the DRE process modifies the sidewall profile slightly, for simplicity, we take the top and bottom diameters as 85% and 60% of the period, respectively. The ratios roughly agree with the dimensions of fabricated SiNH arrays shown in 2c. The period of choice varies from 300 to 1200 nm, and the nanohole depth from 1 to 5 μm. As shown in Figure 8(b), a maximum photocurrent of >45 mA/cm^2 is achieved with a wafer thickness of 200 μm for periods between 700 and 900 nm and a depth above 700 nm because of superior anti-reflection for optically thick wafers. Therefore, a nanohole depth of 700 nm is sufficient to harvest most of the sunlight without auxiliary surface recombination with deeper holes. For thin wafers, the nanohole structures are effective to provide both anti-reflection and light trapping, particularly when microscale textures based on alkaline anisotropic etching are no longer applicable. Figure 8(c) shows that an optimal photocurrent, as high as 36 mA/cm^2, is still possible with a wafer thickness of 5 μm, which occurs at a depth of 750 nm and a period ranging from 700 to 900 nm. It is illustrative from the plot that the periodicity of nanohole arrangement must be around the wavelengths of interests for thin-silicon wafers. Moreover, deeper holes do not result in a higher photocurrent output in a 5-μm-thick wafer because of a reduced active material volume and an increased parasitic absorption loss to the back aluminum contact. Figure 8(d) shows the calculated wafer thickness dependence of the J_{sc} diagram for the flat reference with a single-layer SiN_x anti-reflective coating ($J_{sc,flat}$) and for SiNH arrays with a period of 800 nm and depth of 750 nm ($J_{sc,\ SiNH}$). To examine the differences for thin-substrate devices, an enhancement factor defined as $J_{sc,\ SiNH}/J_{sc,flat}$ is also calculated, as shown in Figure 8 (d). We observed that when wafer thickness is above 100 μm, the changes in the enhancement factor are small and mainly attributed to the anti-reflective property of SiNH arrays. On the other hand, when wafer thickness is below 100 μm, the light-trapping property has considerable influence to optical absorption. Therefore, the excellent photon management capability of SiNH arrays starts to outperform the conventional approach, where an enhancement by as high as 40% is achieved with a wafer thickness of 2 μm. Below 2 μm, the enhancement factor starts to decrease because of the parasitic absorption of the aluminum back contact, which is also a result of strong light trapping. Overall, it is found that SiNH arrays with thickness of 10 μm has an identical current output as the flat surface reference with a typical thickness of 200 μm, indicating a 95% reduction of the material usage.

4. CONCLUSIONS

In summary, solar cells based on silicon nanohole arrays have been demonstrated, which exhibit broadband, omnidirectional anti-reflective properties, and yet sacrificed IQE. A damage removal wet etching was introduced to reduce dry etching-induced surface damages and further suppresses the reflection because of a morphology modification. As a result, the nanohole sample achieved an AM1.5 G spectrum-weighted reflectance of 4.7%, leading to a photocurrent increases from 25.2 mA/cm^2 to 31.5 mA/cm^2 for cell with the damage removal treatment. A comprehensive optical model was also established to study the dimension and wafer thickness dependence of light absorption. The nanohole arrays reveal great potential for light harvesting in thin-silicon substrate with a 95% reduction of material usage compared with a typical cell with a wafer thickness of 200 μm.

ACKNOWLEDGEMENTS

This work is supported by National Science Council (NSC), Taiwan, China under grant number NSC98-2221-E-009-111-MY2.

REFERENCES

1. Lewis NS. Toward cost-effective solar energy use. *Science* 2007; **315**: 798.
2. Catchpole KR, Polman A. Plasmonic solar cells. *Optics Express* 2008; **16**: 21793.
3. Green MA, Basore PA, Chang N, Clugston D, Egan R, Evans R, Hogg D, Jarnason S, Keevers M, Lasswell P, O'Sullivan J, Schubert U, Turner A, Wenham SR,

Young T. Crystalline silicon on glass (CSG) thin-film solar cell modules. *Solar Energy* 2004; **77**: 857.
4. Lu Y, Lal A. High-efficiency ordered silicon nano-conical-frustum array solar cells by self-powered parallel electron lithography. *Nano Letters* 2010; **10**: 4651.
5. Garnett EC, Yang P. Silicon nanowire radial p–n junction solar cells. *Journal of the American Chemical Society* 2008; **130**: 9224.
6. Tian B, Zheng X, Kempa TJ, Fang Y, Yu N, Yu G, Huang J, Lieber CM. Coaxial silicon nanowires as solar cells and nanoelectronic power sources. *Nature* 2007; **449**: 885.
7. Peng KQ, Wang X, Li L, Wu XL, Lee ST. High-performance silicon nanohole solar cells. *Journal of the American Chemical Society* 2010; **132**: 6872.
8. Jung JY, Guo Z, Jee SW, Um HD, Park KT, Lee JH. A strong antireflective solar cell prepared by tapering silicon nanowires. *Optics Express* 2010; **18**: A286.
9. Li Y, Zhang J, Yang B. Antireflective surfaces based on biomimetic nanopillared arrays. *Nano Today* 2010; **5**: 117.
10. Chen C, Jia R, Yue HH, Li HF, Liu XY, Wu DQ, Ding WC, Ye TC, Kasai S, Tamotsu H, Chu JH, Wang SL. Silicon nanowire-array-textured solar cells for photovoltaic application. *Journal of Applied Physics* 2010; **108**: 094318.
11. Yoo J. Reactive ion etching (RIE) technique for application in crystalline silicon solar cells. *Solar Energy* 2010; **84**: 730.
12. Yoon HP, Yuwen YA, Kendrick CE, Barber GD, Podraza NJ, Redwing JM, Mallouk TE, Wronski CR, Mayer TS. Enhanced conversion efficiencies for pillar array solar cells fabricated from crystalline silicon with short minority carrier diffusion lengths. *Applied Physics Letters* 2010; **96**: 213503.
13. Xiong Z, Zhao F, Yang J, Hu X. Comparison of optical absorption in Si nanowire and nanoporous Si structures for photovoltaic applications. *Applied Physics Letters* 2010; **96**: 181903.
14. Han SE, Chen G. Optical absorption enhancement in silicon nanohole arrays for solar photovoltaics. *Nano Letters* 2010; **10**: 1012.
15. Peng K, Xu Y, Wu Y, Yan Y, Lee ST, Zhu J. Aligned single-crystalline si nanowire arrays for photovoltaic applications. *Small* 2005; **1**: 1062.
16. Garnett E, Yang P. Light trapping in silicon nanowire solar cells. *Nano Letters* 2010; **10**: 1082.
17. Yooa J, Yua G, Yib J. Black surface structures for crystalline silicon solar cells. *Materials Science and Engineering B* 2009; **159**: 333.
18. Kumaravelu G, Alkaisi MM, Bittar A, Macdonald D, Zhao J. Damage studies in dry etched textured silicon surfaces. *Current Applied Physics* 2004; **4**: 108.
19. Steinert M, Acker J, Oswald S, Wetzig K. Study on the mechanism of silicon etching in HNO_3-rich HF/HNO_3 mixtures. *Journal of Physical Chemistry C* 2007; **111**: 2133.
20. Ok YW, Rohatgi A, Kil YH, Park SE, Kim DH, Lee JS, Choi CJ. Abnormal dopant distribution in $POCl_3$-diffused n^+ emitter of textured silicon solar cells. *IEEE Electron Device Letters* 2011; **32**: 351.
21. Li H, Jia R, Chen C, Xing Z, Ding W, Meng Y, Wu D, Liu X, Ye T. Influence of nanowires length on performance of crystalline silicon solar cell. *Applied Physics Letters* 2011; **98**: 151116.
22. Toor F, Branz HM, Page MR, Jones KM, Yuan HC. Multi-scale surface texture to improve blue response of nanoporous black silicon solar cells. *Applied Physics Letters* 2011; **99**: 103501.
23. Pang SW, Rathman DD, Silversmith DJ, Mountain RW, DeGraff PD. Damage induced in Si by ion milling or reactive ion etching. *Journal of Applied Physics* 1983; **54**: 3272.
24. Schmidt J, Kerr M, Cuevas A. Surface passivation of silicon solar cells using plasma-enhanced chemical-vapour-deposited SiN films and thin thermal SiO_2/ plasma SiN stacks. *Semiconductor Science and Technology* 2001; **16**: 164.
25. Zaidi SH, Ruby DS, Gee JM. Characterization of random reactive ion etched-textured silicon solar cells. *IEEE Transactions on Electron Devices* 2001; **48**: 1200.
26. Jacobsson R, Mrtensson JO. Evaporated inhomogeneous thin films. *Applied Optics* 1966; **5**: 29.
27. Breitenstein O, Heydenreich J. Non-ideal I–V characteristics of block-cast silicon solar cells. *Solid State Phenomena* 1994; **37**: 139.
28. Kühn R, Fath P, Bucher E. Effects of p–n junction bordering on surfaces investigated by means of 2D-modeling, 28th IEEE PVSC. *Anchorage* 2000; 116.
29. Breitenstein O, Bauer J, Lotnyk A, Wagner JM. Defect induced non-ideal dark I–V characteristics of solar cells. *Superlattices and Microstructures* 2009; **45**: 182.
30. ASTMG173-03. Standard tables for reference solar spectral irradiances, ASTM International, West Conshohocken, Pennsylvania. 2005.
31. Moharam MG, Gaylord TK. Rigorous coupled-wave analysis of planar-grating diffraction. *Journal of the Optical Society of America* 1981; **71**: 811.
32. Moharam MG, Gaylord TK. Diffraction analysis of dielectric surface-relief gratings. *Journal of the Optical Society of America* 1982; **72**: 1385.